Journal of the Meteorological Society of Japan

EARLY ONLINE RELEASE

The DOI for this manuscript is

DOI:10.2151/jmsj.2022-041

J-STAGE Advance published date: June 30th, 2022

The final manuscript after publication will replace the preliminary version at the above DOI once it is available.

Multiple Dynamics of Precipitation Concentrated on the North Side of Typhoon Hagibis (2019) during Extratropical Transition

Wataru YANASE, Kentaro ARAKI, Akiyoshi WADA, Udai SHIMADA, Masahiro HAYASHI

Meteorological Research Institute, Japan Meteorological Agency, Tsukuba, Japan

and

Takeshi HORINOUCHI

Faculty of Environmental Earth Science, Hokkaido University, Sapporo, Japan

June 19, 2022

Corresponding author: Wataru Yanase, Meteorological Research Institute, Japan Meteorological Agency, 1-1, Nagamine Tsukuba, Ibaraki 305-0052, Japan.
E-mail: wtryanase@gmail.com

Abstract

Torrential rain in Typhoon Hagibis caused a devastating disaster in Japan in October 2019. The precipitation was concentrated in the northern half of Hagibis during extratropical transition (ET). To elucidate the mechanisms of this asymmetric precipitation, synoptic- and meso-scale processes were analyzed mainly using the Japan Meteorological Agency Non-Hydrostatic Model. The present study demonstrates that the asymmetric processes were different depending on the ET stages. When Hagibis was close to the baroclinic zone at middle latitudes around 12 October (the frontal stage), heavy precipitation in the northeastern part of Hagibis was attributed to warm frontogenesis and a quasi-geostrophic ascent, as reported in many previous studies. In contrast, when Hagibis was moderately distant from the baroclinic zone around 11 October (the prefrontal stage), heavy precipitation in the northern part occurred in slantwise northward ascending motion in the outer region. This slantwise motion developed in a region with strong westerly vertical shear, which was enhanced between Hagibis and a westerly jet stream. Based on the analyses of potential vorticity and absolute angular momentum, this region was characterized by reduced moist symmetric stability in the lower and middle troposphere accompanied by inertial instability in the upper troposphere and conditional instability in the lower troposphere. These results provide additional insights into the

time evolution of asymmetric processes during ET in the absence of a distinct upper-tropospheric trough, particularly the slantwise motion in the prefrontal stage.

Keywords tropical cyclone; extratropical transition; cloud resolving simulation

1. Introduction

In October 2019, torrential rain in Typhoon Hagibis caused more than 100 fatalities mainly in the eastern part of Honshu, Japan's largest island. It was one of the nation's most devastating typhoon disasters in recent decades. Takemi and Unuma (2020) attributed the large amount of precipitation to high humidity and moist absolute unstable layers (MAUL). Kawase et al. (2021) demonstrated that the atmospheric and oceanic warming trends for 40 years enhanced the precipitation. From the perspective of disaster prevention, it is also important to understand where in the cyclone the large amount of precipitation was concentrated. When Hagibis approached Japan, most of the precipitation was concentrated in its northern half (Fig. 1b, c). This remarkably asymmetric structure commenced to develop a few days before Hagibis became an extratropical cyclone to the east of Honshu at 0300 UTC 13 October. Fig. 1

Extratropical transition (ET) is the process, typically a few tens of hours long (Evans and Hart 2003; Kitabatake 2011), in which a tropical cyclone (TC) transforms into an extratropical cyclone in a baroclinic environment at middle latitudes (Jones et al. 2003; Evans et al. 2017). As ET is a gradual process, its conceptual model considers the onset and completion of ET (Evans and Hart 2003; Jones et al. 2003); the completion approximately corresponds to the time when an operational forecast center declares that a TC has changed into an extratropical cyclone. Between the onset and completion of ET, a TC generally starts to take on an asymmetric structure (Klein et al. 2000; Evans and Hart 2003; Jones et al. 2003). Therefore, the asymmetric precipitation in Hagibis around Japan appears to have been associated with ET processes.

In-situ and remote sensing observations have documented asymmetric patterns of cloud and precipitation of TCs during ET (Kitabatake 2008; Quinting et al. 2014; Katsumata et al. 2016). Klein et al. (2000) proposed a conceptual model of TC structures during ET, including warm frontogenesis, a cloud band, a cirrus edge, and a dry slot, which are partly similar to the structures of ordinary extratropical cyclones. A delta rain shield is a delta-shaped precipitation system from 200 to 500 km north of a cyclone center, which is unique to a TC approaching the baroclinic zone (Shimazu 1998). As ET proceeds, the distribution of heavy precipitation tends to be concentrated to the left of the track of a TC (Jones et al. 2003; Atallah et al. 2007; Deng and Ritchie 2018). Atallah et al. (2007) attributed this distribution to an influence of midlatitude upper-tropospheric troughs northwest of TCs during ET. Upper-tropospheric troughs often force an ascent on their east sides promoting formation of asymmetric structures of TCs during ET (Kitabatake 2002; Kitabatake et al. 2007; Galarneau et al. 2013; Yanase et al. 2020). However, an upper-tropospheric trough was indistinct northwest of Hagibis as shown later, indicating that other processes were responsible for concentrating the heavy rainfall.

Frontal dynamics is an important process for a TC during ET, which tends to form a strong warm front and a weak cold front (Harr and Elsberry 2000; Klein et al. 2000; Kitabatake 2008). Frontal dynamics may also vary from one case to another; Hagibis had a warm front on its northeast side (Iizuka et al. 2021), whereas Hurricane Sandy (2012), a high-impact ET case in the North Atlantic, had a warm front on its northwest side (Galarneau et al. 2013). In addition, as precipitation systems in Hagibis were observed in different locations depending on time (Fig. 1b, c), the relationship between precipitation and frontal dynamics may change at different ET stages.

A tilt of a vortex due to vertical shear also causes asymmetry of vertical motion through several processes (Jones 1995; Ueno 2007; Riemer et al. 2010); a vortex tilt forces an ascent with adiabatic cooling on the downshear side of the vortex due to thermal wind adjustment (Fig. 4b in Jones 1995); the resultant temperature anomaly associated with the vortex tilt modifies isentropic surface on which cyclonic circulation is accompanied by vertical motion (Fig. 4c in Jones 1995); a lower part of the tilted vortex forces an ascent due to the Ekman pumping process (Riemer et al. 2010). These processes generally accentuates precipitation on the downshear to downshear-left side (Ueno 2007; Kwon and Frank 2008). Because the vortex-tilt mechanism is associated with a strong vortex in a TC core (several tens $\sim$ 200 km), asymmetric ascending motion and precipitation also occur around the core region (Ueno 2007, 2008; Riemer et al. 2010), which are much smaller than the asymmetric structures caused by baroclinic process (Yanase and Niino 2019).

A westerly jet stream north of a TC enhances northward outflow in the upper troposphere. From the perspective of the zonal momentum equation, Saito (2019) analyzed the relationship between the northward ageostrophic flow and the acceleration of zonal wind for a flow from a TC to a jet stream. From the perspective of the inertial stability of horizontal flow, idealized experiments demonstrated that the northward outflow from a TC was enhanced due to weak inertial stability on the anticyclonic shear side (i.e. south side) of a westerly jet stream (Rappin et al. 2011; Komaromi and Doyle 2018). Ito and Ichikawa (2021) confirmed this enhancement for the case of Hagibis in their numerical simulation. Recently, Dai et al. (2019) demonstrated that a jet stream affected not only upper-tropospheric outflow but also deep convection throughout the troposphere.

The purpose of this paper is to describe the asymmetric structures of

Hagibis during ET based on observations and analysis datasets, and to elucidate their mechanisms based on numerical simulations. We first examined frontal dynamics which have played important roles in many previous ET cases. As we found characteristics that were not explained by frontal dynamics alone, we also explored other candidates for asymmetric mechanisms. Section 2 of this paper describes the dataset used for the analysis and the design of the numerical simulations. Section 3 presents characteristics of Hagibis based on observations and reanalysis. Section 4 analyzes the structures and dynamics of Hagibis based on numerical simulations. Section 5 discusses the possible mechanisms of asymmetric precipitation, and Section 6 summarizes the main conclusion.

2. Methodology

2.1 Observations and analysis datasets

The best track product by the Japan Meteorological Agency (JMA) was used for the locations and minimum sea level pressure of Hagibis (Japan Meteorological Agency 2020). Surface weather charts were also provided by the JMA.

Synoptic conditions around Hagibis were examined using the JRA-55 reanalysis data (Kobayashi et al. 2015) with a horizontal grid spacing of

1.25°. The reanalysis is produced based on a global atmospheric model with a TL319 spectral horizontal resolution and 60 vertical levels, and on the four-dimensional variational data assimilation (4D-Var) of the JMA.

The Radar/Raingauge-Analyzed Precipitation is a 1-km-grid dataset based on ground-based precipitation and radar observations in Japan (Ishizaki and Matsuyama 2018). High-frequency microwave (∼90 GHz) satellite imagery provided by the Naval Research Laboratory (2019), which indicates scattering by large precipitation particles, especially by snowflakes, was used for presenting the time evolution of asymmetric precipitation systems in Hagibis, as shown in Fig. 1.

The Atmospheric Motion Vector (AMV) dataset is a horizontal wind product that is derived from Himawari-8 geostationary satellite observations by tracking the patterns of clouds and water vapor (Shimoji 2017). We utilized four infrared band observations (6.2, 6.9, 7.3 and 10.4 μm wavelength) at 2.5-min intervals. We extracted horizontal winds at upper levels that were estimated from the observed radiance and the atmospheric variables of the JMA global atmospheric model with a TL959 spectral horizontal resolution.

2.2 *Numerical model and experimental design*

To analyze the asymmetric dynamics of Hagibis, we conducted numerical simulations using the JMA Nonhydrostatic Model (JMA-NHM; Saito et al. 2006). The cloud processes were simulated by a two-moment bulk-type microphysics scheme that calculated mixing ratios for cloud water, cloud ice, rain, snow, and graupel as well as number concentrations for cloud ice, snow, and graupel (Lin et al. 1983; Murakami 1990), whereas no cumulus parameterization was used. The planetary boundary layer was parameterized by the level-2.5 closure of the Mellor-Yamada-Nakanishi-Niino turbulence scheme (Nakanishi and Niino 2004) with the surface-layer scheme proposed by Beljaars (1995). The model also calculated long-wave and short-wave radiation processes and ground temperature as described in Japan Meteorological Agency (2013).

The horizontal grid spacing was 2 km for a domain of 4000 km $\times$ 4000 km centered at 35°N, 140°E based on the Lambert conformal conical projection (Fig. 2a). The vertical grid spacing for 48 layers with the model top at 21801 m above sea level (ASL) increased linearly from 40 m at the lowest level to 868 m at the highest level. Fig. 2

The initial and boundary conditions were obtained by interpolating the global analysis data provided by the JMA (Japan Meteorological Agency 2019). The 6-hourly atmospheric analysis was produced based on a global spectral model with a TL959 spectral horizontal resolution (roughly equivalent to 0.1875°) and 100 vertical levels together with the 4D-Var, whereas the daily sea surface temperature (SST) analysis was the Merged satellite and in situ data Global Daily SST (MGDSST) dataset (Kurihara et al. 2006) with a horizontal grid spacing of 0.25°.

The simulation with the full physics and the real topography is referred to as the control experiment (CTL). As the orography around Japan (Fig. 2a) may affect vertical motion and precipitation of TCs (Murata 2009; Lentink et al. 2018), we also conducted a sensitivity experiment in which Honshu, Hokkaido, Shikoku, Kyushu and other neighboring small islands were replaced by the ocean surface with no orography (contours in Fig. 3b, c). The SST was linearly interpolated in the zonal direction between the eastern and western coasts of the islands. This experiment is referred to as NIS. Time integration was conducted at time steps of 10 s for 72 h starting at 1200 UTC 10 October. Fig. 3

2.3 Analyses of atmospheric dynamics

A center of the cyclone was defined by the location of minimum sea level pressure. Environmental vertical shear was defined by the difference in horizontal wind between 1450 and 12130 m ASL ($\sim$850 and $\sim$200 hPa, respectively) averaged between 200 and 800 km radius from the cyclone center.

In the following analyses, we mainly analyzed a 10-km-grid dataset that was created by averaging 5 $\times$ 5 grids of the original 2-km-grid dataset, because the 2-km-grid dataset was too noisy to analyze the asymmetric structures of Hagibis. In addition, if not otherwise specified, the 10-km-grid dataset was further smoothed using a 100-km binomial filter, which calculates a weighted mean with 11-point binomial coefficients in the horizontal directions.

A scalar frontogenesis analysis assesses the cause of the temporal change in the magnitude of horizontal gradient of θ (Keyser et al. 1988; Schultz and Doswell 1999), where θ is usually potential temperature or equivalent potential temperature (EPT). The scalar frontogenesis is determined by three terms in the following equation (Schultz and Doswell 1999):

$$\frac{d}{dt}|\boldsymbol{\nabla_h}\theta| = \frac{1}{2}|\boldsymbol{\nabla_h}\theta| E\cos 2\beta - \frac{1}{2}|\boldsymbol{\nabla_h}\theta|(\boldsymbol{\nabla_h}\cdot\boldsymbol{V_h}) - \frac{\partial\theta}{\partial z}\left(\boldsymbol{\nabla_h} w \cdot \frac{\boldsymbol{\nabla_h}\theta}{|\boldsymbol{\nabla_h}\theta|}\right), \quad (1)$$

where $\boldsymbol{\nabla_h}$ is the horizontal gradient operator, E is the resultant deformation defined as

$$E = \left\{\left(\frac{\partial u}{\partial x} - \frac{\partial v}{\partial y}\right)^2 + \left(\frac{\partial v}{\partial x} + \frac{\partial u}{\partial y}\right)^2\right\}^{1/2}, \quad (2)$$

β is the local angle between an isoline of θ and the dilatation axis, $\boldsymbol{V_h}$ is the horizontal wind vector, and w is the vertical wind. On the right-hand side of Eq. (1), the first term indicates a deformation effect, which causes frontogenesis (frontolysis) if the angle between the isoline of θ and the dilatation axis of the horizontal wind is smaller (greater) than 45°. The second term indicates a divergence effect, which causes frontogenesis (frontolysis) if the horizontal flow converges (diverges) in the horizontal gradient of θ; note that convergence and divergence of horizontal flow in the lower troposphere correspond to ascending and descending motion aloft, respectively, because of the conservation of mass. The third term indicates a tilting effect, which causes frontogenesis (frontolysis) if warm air descends (ascends) and cold air ascends (descends); in other words, frontogenesis (frontolysis) occurs in a thermally indirect (direct) circulation.

To examine a secondary circulation linked to vertical motion, we decomposed the horizontal winds (referred to as total winds) into divergent and non-divergent winds instead of radial and azimuthal winds because the atmospheric flow was not axisymmetric. The non-divergent winds was expressed as the derivatives of a stream function, whereas the divergent wind was the difference between the total winds and the non-divergent winds; the stream function was obtained from the total wind by applying a relaxation method to Poisson's equation.

We also decomposed the total winds into geostrophic and ageostrophic winds, and into gradient and non-gradient winds, based on the locally determined balanced equation,

$$\frac{V_b^2}{r_b} + fV_b = \frac{1}{\rho}\frac{\partial p}{\partial n}, \tag{3}$$

where V_b is the balanced wind speed parallel to the isobar, r_b is the radius of curvature of the isobar, f is the Coriolis parameter, ρ is the density, p is the pressure, and n is the unit vector perpendicular to the isobar. Geostrophic winds were obtained by neglecting the first term on the left-hand side, and ageostrophic winds were the difference between the total and geostrophic winds. The radius of curvature r_b was locally determined from the shape of the isobars as in Endlich (1961), although we neglected the time derivative terms. Given r_b, the gradient wind was obtained by the quadratic formula of Eq. (3); for a strong anticyclonic flow, the gradient wind was indeterminate due to complex roots of the quadratic formula (Knox and Ohmann 2006). The data were smoothed by a 2000-km binomial filter.

Potential vorticity (PV) diagnoses symmetric stability. Moist PV (P_m) is defined as

$$P_m = \frac{\boldsymbol{\zeta_a} \cdot \boldsymbol{\nabla}\theta_e^*}{\rho}, \tag{4}$$

where $\boldsymbol{\zeta_a}$ is the absolute vorticity vector, $\boldsymbol{\nabla}$ is the three-dimensional gradient operator, θ_e^* is the saturation EPT (SEPT), and ρ is the density. Dry PV (P_d) is defined as

$$P_d = \frac{\boldsymbol{\zeta_a} \cdot \boldsymbol{\nabla}\theta_d}{\rho}, \tag{5}$$

where θ_d is potential temperature.

3. Observations and reanalysis

The locations and minimum sea level pressure of Hagibis in the best track product are shown in Fig. 2. After Hagibis became a tropical storm (winds $\geq$ 34 kt) at 15.1°N, 157.4°E at 1800 UTC 5 October 2019 (not shown), it rapidly intensified to its maximum intensity of 915 hPa from 1200 UTC 7 October to 0600 UTC 10 October. During the mature stage, Hagibis had a clear eye at its center and a relatively axisymmetric pattern (Fig. 1a). After 0600 UTC 10 October, Hagibis started to decay (Fig. 2b) during its northward motion, and finally became an extratropical cyclone at 0300 UTC 13 October. During this period, Hagibis developed an asymmetric structure with most of its precipitation systems concentrated in its northern half (Fig. 1b, c); from 11 to 13 October, the dominant area of precipitation system shifted from the northern part to the northeastern part.

Figure 3a shows precipitation accumulated between 1200 UTC 10 October and 1200 UTC 13 October; this period corresponds to the integration time of the simulation and includes the time when Hagibis caused heavy rainfall in Honshu. The precipitation was also asymmetric, concentrated to the left of the track of Hagibis. Whereas part of this asymmetry appears to arise from the orography in Honshu (Fig. 2a), it was also observed over the ocean. A sensitivity experiment in Section 4 examines to what extent this asymmetry was caused by orography. The left-of-track precipitation pattern was consistent with previous studies of ET or recurving TCs (Jones et al. 2003; Atallah et al. 2007; Deng and Ritchie 2018).

Synoptic conditions may provide some clues about the asymmetric dynamics of Hagibis. Figure 4a–c shows JMA's surface weather charts. At 1200 UTC 11 October, a front accompanied by a preceding low pressure system was located around 40°N, far north of the center of Hagibis (Fig. 4a). At 1200 UTC 12 October, the front was located northeast of Hagibis (Fig. 4b), when precipitation shifted to the northeastern part (Fig. 1c). This front finally became a warm front accompanying the extratropical cyclone transitioned from Hagibis (ex-Hagibis) at 1200 UTC 13 October (Fig. 4c). The Q vector analysis indicates a quasi-geostrophic ascent in the northeastern part (Supplement 1). Thus, the relationship between the precipitation, the front, and the quasi-geostrophic ascent in the northeastern part of Hagibis and ex-Hagibis after 12 October resembled the characteristics of ordinary extratropical cyclones. Fig. 4

Figure 4d–f shows PV and horizontal wind speed on the 340 K isentropic surface, which corresponded to 200–300 hPa in the middle latitudes in October 2019. On 11 and 12 October, there was no distinct upper-tropospheric trough around Hagibis (Fig. 4d-e). Thus, the precipitation concentrated in the northern half during this period was not fully explained by quasi-geostrophic forcing of upper-tropospheric troughs. From 11 to 12 October, the westerly jet stream was enhanced northeast of Hagibis presumably owing to the interaction between the TC and a jet stream (Keller et al. 2019). On 13 October, Hagibis approached the jet stream and the steep gradient of PV in the upper troposphere (Fig. 4f).

4. Numerical simulations

In this section we first validate the track, intensity and precipitation of Hagibis in the simulation, and then we examine the influence of frontal dynamics and other processes on the asymmetric structure.

4.1 Time evolution of asymmetric precipitation

The track of Hagibis in the CTL experiment was in good agreement with that recorded in the best track analysis between 1200 UTC 10 October and 1200 UTC 13 October (Fig. 2a); during the poleward motion in this period, Hagibis recurved from northwestward to northeastward in the latter half of 11 October, made landfall on Honshu on 12 October, then moved northeastward over the Pacific Ocean. Hagibis was weakening during this period as recorded in both CTL and the best track analysis (Fig. 2b), although CTL overestimated the intensity of Hagibis at an earlier integration. This overestimation may have originated in the SST obtained from the MGDSST dataset, which tends to underestimate ocean cooling induced by TCs (Kunii et al. 2017).

To examine the time evolution of asymmetric precipitation, we show the horizontal distribution of the total condensed water path (TCWP; the sum of cloud water, cloud ice, rain, snow, and graupel integrated vertically through the model domain) in Fig. 5, and the azimuth-time Hovmöller diagram of the TCWP averaged over a 500-km radius from the cyclone center in Fig. 6. After the initial spin up of several hours, the dominant TCWP occurred to the north of Hagibis on 11 October (Figs. 5a, b and 6). At 1200 UTC 11 October, the TCWP formed a delta shape bounded on the northwest side by an arc-like band, which is in good agreement with the microwave satellite observation (Fig. 1b). This distribution resembled the delta rain shield analyzed in Shimazu (1998). Fig. 5

On 12 October (Fig. 5c, d), the dominant TCWP region gradually shifted from the northern part to the northeastern part. This shift was also consistent with the microwave observation (Fig. 1c) and is clearly identified in the Hovmöller diagram (Fig. 6). Environmental vertical shear is a basic parameter responsible for asymmetric dynamics including baroclinic and vortex-tilt mechanisms (Jones 1995). The azimuth of the dominant TCWP was on the left side (downstream in the cyclonic circulation) of the verti- Fig. 6

cal shear vector (circles and crosses in Fig. 6). The azimuthal difference between the TCWP peak and the vertical shear vector was larger on 11 October than on 12 October, implying that the mechanisms of asymmetry were different between those two days.

For more quantitative validation, total precipitation accumulated from 1200 UTC 10 October to 1200 UTC 13 October in CTL and the corresponding radar/rain gauge–analyzed precipitation are compared in Fig. 3a, b. The model reproduced the concentration of precipitation to the left of the track as well as the orographic enhancement in Honshu.

To examine the influence of orography, we compared the CTL and NIS experiments. The track of Hagibis in NIS was nearly the same as in CTL (Fig. 3b, c). The decay rate was slower in NIS than in CTL after 1200 UTC 12 October (Fig. 2b), because the ocean surface was more favorable for maintaining the intensity of Hagibis than the land surface. The asymmetric pattern of TCWP in NIS resembled that in CTL throughout the integration time (Fig. S4 in Supplement 3). The distribution of total precipitation was smoother in NIS than in CTL (Fig. 3b, c), indicating that the orographic effect enhanced local precipitation mainly in Honshu. However, the total precipitation was still largest to the left of the track even in the absence of the orographic effect. Therefore, the remainder of this study focuses on the atmospheric dynamics responsible for the asymmetric precipitation.

4.2 Frontal dynamics

Time evolution of fronts is an important process of ET. Figure 7 shows the horizontal distribution of EPT at 530 m ASL and the magnitude of the horizontal gradient of EPT as a proxy for fronts. On 11 October (Fig. 7a, b), the baroclinic zone at middle latitudes was located around 35°N∼45°N, and was modulated by a preceding low pressure system, which was consistent with the front analyzed in the weather chart (Fig. 4a). Whereas Hagibis was far south of this baroclinic zone it had a local front to the northwest (the label “LF” in Fig. 7b) between the area of high EPT around the cyclone center to the southeast and the area of low EPT to the northwest. This low EPT was confined to a limited area that was separated from the low EPT at higher-latitudes particularly at 0000 UTC 11 October (Fig. 7a). Furthermore, a sensitivity experiment in Supplement 4 demonstrated that asymmetric precipitation formed even in the absence of the local front. Therefore, we have concluded that the local front was not essential for the heavy precipitation concentrated in the northern part of Hagibis.

On 12 October (Fig. 7c, d), the local front merged with the baroclinic zone around Japan. The merged front developed mainly northeast of Hagibis (the label “WF” in Fig. 7d) and finally became a warm front of ex-Hagibis after the ET completion on 13 October (Fig. 7f), as shown in the weather charts (Fig. 4b, c). The merged front northeast of Hagibis is hereafter referred to as a warm front irrespective of the ET completion.

We analyzed the dynamics of the warm front for 1200 UTC 12 October in detail. Because the orographic effect disturbed frontal dynamics, we analyzed the result of the NIS experiment for clarity, in which Hagibis developed the warm front as in CTL (Fig. S5 in Supplement 3). Figure 8 shows atmospheric variables associated with frontal dynamics around Hagibis. The 1-h precipitation was particularly large along the warm front (Fig. 8a). The updrafts in the warm front were organized more tightly than those in a spiral rain band east and southeast of the cyclone center (Fig. 8b). Another precipitation maximum immediately northeast (downshear) of the cyclone center was associated with the decaying asymmetric eyewall (see also Fig. 5). Note that the 1-h precipitation associated with individual convective clouds is elongated in the azimuthal direction, reflecting the cloud motion during an hour. Fig. 7

A scalar frontogenesis analysis given in Eq. (1), the most intense frontogenesis in the warm front was attributed to the deformation effect (Fig. 8d), where the dilatation axes of horizontal flow were parallel to the isolines of EPT (Fig. 8c). The warm front was also enhanced by the divergence effect (Fig. 8e), whereas it was weakened by the tilting effect due to the direct circulation across the front. These characteristics were also identified in the frontogenesis analysis for potential temperature (not shown). Sec- Fig. 8

tion 5 discusses why the deformation effect was large in the northeastern quadrant of Hagibis.

In summary, frontal dynamics was indistinct on 11 October, whereas it was responsible for the precipitation concentrated in the northeastern part on 12 October; hereafter, we refer to the former and the latter as the prefrontal and frontal stages respectively.

4.3 Asymmetric structures in the prefrontal stage

In the prefrontal stage, the dominant precipitation occurred in the northern part of Hagibis (Figs. 5 and 6), and frontal dynamics was not essential. Therefore, we analyzed the structures at 1200 UTC 11 October in CTL in more detail.

Figures 9 and 10 present horizontal and vertical structures of Hagibis, respectively (the meridional ranges are different between the two figures). Ascending motion with diabatic heating to the north of Hagibis was apparently more intense than that to the south (Figs. 9a, b, and 10a). Although it appears to be partly attributed to cyclonic advection of high EPT from low latitudes to the north of Hagibis (see also Fig. 7b), convective available potential energy (CAPE) in this area was not large compared to low latitudes (Fig. 9c), indicating that the ascending motion was not explained by conditional instability alone. Taking a closer look, the ascending motion was intense in two different regions: an inner region including an eyewall within 1° north of the cyclone center and an outer region between 2° and 5°. The ascent in the inner region occurred near the edge of a strong vortex (Figs. 9b, 10b) along with a downshear tilt of the vortex (Fig. S2 in Supplement 2), which is consistent with characteristics of the vortex-tilt mechanism in theoretical, numerical, and observational studies (Jones 1995; Ueno 2007; Foerster et al. 2014). On the other hand, the ascent in the outer region was not associated with a strong vortex of a corresponding horizontal scale, implying dynamics different from the vortex-tilt mechanism. Hereafter, we focus on the ascending motion in the outer region which caused the wide area of TCWP (Fig. 5b). Fig. 9

The ascending motion in the outer region had a slantwise distribution that expanded northward or outward with height (Fig. 10a). Such a slantwise distribution was also observed by the dual-frequency precipitation radar on the Global Precipitation Measurement (GPM) core observatory satellite at 0939 UTC 11 October (Japan Aerospace Exploration Agency 2020). The meridional component of the divergent wind confirms slantwise motion where the ascending motion flowed northward or outward (Fig. 10c). Below this ascending motion, descending motion flowed southward or inward between 3° and 5° north of the cyclone center which was promoted by evaporative cooling (see also Supplement 4). The distribution of the as- Fig. 10

cent and descent was nearly parallel to the isoline of EPT (Fig. 10c). These characteristics provide a clue about the dynamics in the outer region.

We further examined the three-dimensional structure of the slantwise motion by trajectory analyses which started at 1200 UTC 11 October. The trajectory analysis was conducted by applying the fourth-order Runge-Kutta method to the wind field in the 2-km-grid dataset at 1-min intervals. Figure 11a presents backward trajectories that started at 10 km ASL north of the cyclone center and ended below 2 km ASL, indicating ascending motion. Figure 12 shows the relationship between the azimuthal location, radial velocity, and vertical velocity for the same trajectories. Most of the trajectories moved cyclonically on the east side of Hagibis at low levels, then ascended steadily between the northeast and northwest of Hagibis (Figs. 11a and 12b), although some trajectories ascended rapidly (≥ 1 m s^{-1}) due to convection. On the north side of Hagibis, the trajectories also moved outward from the cyclone center (Figs. 11a and 12a). A scatter plot diagram of the radial and vertical velocities indicates that most of the ascending motion was associated with the outward motion (Fig. 12c). Figure 11b presents forward trajectories that started at 1 km ASL around the cyclone center and ended above 10 km ASL, also indicating ascending motion. The trajectories moved cyclonically in the lower troposphere and dominantly ascended in the northern half of the cyclone, consistent with the backward trajectories in Fig. 11a, and then moved further northward in the upper troposphere. Fig. 11

To examine the synoptic conditions around the northward outflow, Fig. 13b shows the horizontal winds at upper troposphere. The outflow from Hagibis moved dominantly northward to a westerly jet stream at higher latitudes, in good agreement with the AMV derived from the Himawari-8 observations (Fig. 13a). The decomposition into geostrophic and ageostrophic winds indicates that the northward outflow was associated with the ageostrophic wind (Fig. 13c, d). Whereas the geostrophic wind provided a good approximation of the jet stream, it overestimated the cyclonic wind around Hagibis because the centrifugal force in a curved flow was neglected (compare Fig. 13b and 13c). As a result, the ageostrophic wind around Hagibis shows a strong anticyclonic flow. The decomposition into gradient and non-gradient winds allowed us to incorporate the effect of the centrifugal force. Because the gradient wind provided a good approximation of the cyclonic flow (not shown), the non-gradient wind was small near the cyclone center (Fig. 13e). This decomposition also confirms that the northward outflow was associated with the unbalanced (non-gradient) wind. Thus, the northward divergent wind in Figs. 10c and 13f was part of the unbalanced flow between Hagibis and the jet stream. Fig. 13

Fig. 12

4.4 Stability of the motion in the prefrontal stage

In the prefrontal stage, as shown in the previous section, the precipitation concentrated to the north of Hagibis was associated with the slantwise ascending motion between Hagibis and the westerly jet stream. Figure 14 shows meridional-vertical section through the cyclone center for CTL at 1200 UTC 11 October. The zonal wind around Hagibis appears to be a merger of the winds associated with the cyclone and a westerly jet stream to the north (Fig. 14a). In particular, the vertical shear of the zonal wind was stronger on the north side of Hagibis than on the south side. To understand a link between the slantwise motion and the vertical shear, we assessed symmetric stability (Holton 2004; Schultz and Schumacher 1999). Fig. 14

Moist symmetric stability can be diagnosed by moist PV (P_m) in Eq. (4). Negative P_m denotes moist symmetric instability. The special case of moist symmetric instability is conditional instability, which is indicated by a negative vertical gradient of SEPT (Schultz and Schumacher 1999). Figure 14b depicts moist symmetric instability, weak symmetric stability, and conditional instability in different colors. The north side of Hagibis was characterized by not only conditional instability but also moist symmetric instability and weak symmetric stability, particularly around 2°–4° north of the cyclone center. Conditional instability around 1°∼3° north of the cyclone center was associated with moderate CAPE (Fig. 9c) and MAUL analyzed in Takemi and Unuma (2020). Schultz and Schumacher (1999) noted that the coexistence of conditional instability and moist symmetric instability is often observed. As moist symmetric stability was obscured or canceled by conditional stability, Fig. 14c presents the contribution of horizontal vorticity and horizontal gradient of SEPT to P_m in Eq. (4), which is dependent on vertical shear but independent of conditional stability. This analysis confirms that the strong vertical shear robustly reduced P_m on the north side of the cyclone center.

Finally, adiabatic dynamics of the unsaturated atmosphere in the upper troposphere was diagnosed by dry PV (P_d) in Eq. (5). Regions with negative P_d values, which indicate dry symmetric instability, were present 4° or further north of the cyclone center in the upper troposphere (Fig. 14d), where northward flow was intense (Fig. 10c). Moreover, this region was characterized by negative absolute vorticity (Fig. 10b) indicating inertial instability, which was also reported by Ito and Ichikawa (2021). Note that symmetric instability includes inertial instability as a special case (e.g., Holton 2004).

In summary, the slantwise motion in the lower and middle troposphere occurred in an environment with reduced moist symmetric stability due to strong westerly vertical shear between Hagibis and the westerly jet stream. The reduced moist symmetric stability was also confirmed by absolute angular momentum analysis in Appendix A. The characteristics indicate in the meridional section was robustly observed in the azimuthally averaged fields in the northern and southern quadrants (Fig. S3 in Supplement 2).

5. Discussion

In this section we discuss the asymmetric processes of Hagibis in the frontal and prefrontal stages on the basis of previous studies including the conceptual model of TC structures during ET (Klein et al. 2000; Areas 1–5 in their Fig. 5) and dynamic theories.

5.1 Asymmetric dynamics in the frontal stage

In the frontal stage, when Hagibis approached the baroclinic zone at middle latitudes around 12 October, precipitation became dominant in the northeastern part of Hagibis (Figs. 5d and 6), near the warm front (Fig. 7d) and near the convergence of the Q vector (Fig. S1b in Supplement 1). The warm front developed mainly through the deformation effect (Fig. 8) after the local front merged with the baroclinic zone. Note that frontogenesis is also dynamically linked to the Q vector in the particular case of adiabatic and quasi-geostrophic horizontal flow (Keyser et al. 1988; Kitabatake 2002) These characteristics were in good agreement with the ascent in Area 4 in Klein's conceptual model, where a warm conveyor belt ascends over sloped isentropic surfaces associated with a warm front.

Previous studies have reported that warm frontogenesis is dominant over cold frontogenesis for ET cases (Klein et al. 2000; Kitabatake 2008; Quinting et al. 2014) including Hagibis (Iizuka et al. 2021). Our frontogenesis analysis demonstrated that the warm front was enhanced by the deformation effect northeast of Hagibis, where the dilatation axes were nearly parallel to the isolines of EPT. The importance of the deformation effect was also consistent with Kitabatake (2008). Divergence and tilting effects played positive and negative roles, respectively, in the warm frontogenesis. These two effects are linked to vertical motion, causing some feedback processes between a front and ascending motion; in particular, the tilting term provides negative feedback if the vertical motion is a thermally direct circulation across the front in a stable atmosphere.

The warm frontogenesis northeast of Hagibis was different from that northwest of Hurricane Sandy (2012) analyzed by Galarneau et al. (2013). If a deep upper-tropospheric trough exists northwest of a TC as in Sandy, the juxtaposition of a cold core of the upper-tropospheric trough and a warm core of the TC tends to enhance temperature gradient northwest of the TC (Atallah et al. 2007). If a deep upper-tropospheric trough is absent as in Hagibis, on the other hand, the warm frontogenesis northeast of a TC may be explained by an interaction between a cyclonic vortex and a baroclinic environment (Keyser et al. 1988) for a simplified ET situation (see Appendix B).

5.2 Asymmetric dynamics in the prefrontal stage

In the prefrontal stage, when Hagibis was moderately distant from the baroclinic zone around 11 October, precipitation was mainly concentrated in the northern part of Hagibis (Figs. 5b and 6). The ascending motion was not explained by quasi-geostrophic ascent (Supplement 1) or by frontal dynamics (Section 4.2 and Supplement 4). The vortex-tilt mechanism (Jones 1995; Ueno 2007) explains the ascent in the inner region, but not in the outer region (Figs. 9, 10, S2).

The structures in the outer region was in good agreement with the characteristics of a TC under the influence of a westerly jet stream to the north (Rappin et al. 2011; Komaromi and Doyle 2018). In the upper troposphere, a northward unbalanced outflow was enhanced from the TC to the jet stream (Fig. 13), which was associated with negative absolute vorticity implying inertial instability (Fig. 10b). Furthermore, the three dimensional structures resembled the conceptual model of enhanced outer rainband under the influence of a westerly jet stream proposed by Dai et al. (2019; their Fig. 15), which compared TCs in idealized experiments with and without a jet stream; the jet stream enhanced deep slantwise convection outside an eyewall with outward ascending motion and inward descending motion along the isentropic surface (compare our Fig. 10 with their Figs. 5 and 6); trajectories indicate that this slantwise ascending motion was an important contributor to the outflow in the upper troposphere (compare our Fig. 11b with their Fig. 7). The structures also resembled the ascent in Area 5 in Klein's conceptual model in that air parcels ascend over a tilted isentropic surface in a cloud band northwest of a TC, and turn their path from cyclonic motion in the lower troposphere to outward motion in the upper troposphere. Note that this slantwise ascent associated with outward motion appears to be different from that associated with cyclonic motion on a tilted isentropic surface due to an asymmetric TC structure in the vortex-tilt mechanism (e.g., Fig. 4c in Jones 1995; trajectory analysis in Ueno 2008), or due to a baroclinic zone in the warm-advection mechanism (e.g., Fig. 4a in Jones 1995).

Given a deep northward ascending motion in the outer region, we expanded the TC-jet interaction mechanism from inertial stability for horizontal motion in the upper troposphere to symmetric stability for three dimensional motion throughout the troposphere (Fig. 15). When there is a jet stream with westerly vertical shear (the blue circled dots) to the north of a TC, it enhances the westerly vertical shear associated with the TC (the red circled crosses). The meridional temperature gradient is also enhanced to the north of the TC because of thermal wind balance. The enhanced vertical shear and meridional temperature gradient reduce symmetric stability, promoting slantwise motion. On the other hand, the easterly vertical shear on the south side of the TC (the red circled dots) is distant from the jet stream and opposes the westerly vertical shear of the jet stream, which is not favorable for slantwise motion. Fig. 15

Because moist symmetric stability is a combination of inertial stability and conditional stability, the reduced moist symmetric stability north of Hagibis is considered to have been linked to inertial instability in the upper troposphere (Ito and Ichikawa 2021) and conditional instability or MAUL in the lower troposphere (Takemi and Unuma 2020). It is important to understand the contribution of these processes and interaction between them in future study.

6. Summary

Typhoon Hagibis was accompanied by heavy precipitation concentrated in its northern half when it caused a devastating disaster in Honshu in October 2019. A sensitivity experiment confirmed that the orographic effect was not essential for the asymmetric precipitation, although it locally enhanced precipitation near the mountains. Therefore, we explored atmospheric dynamics responsible for the asymmetric precipitation during the

ET. In the absence of a distinct upper-tropospheric trough, the baroclinic zone at middle latitudes north of Hagibis played different roles depending on the distance from Hagibis.

When Hagibis was close to the baroclinic zone around 12 October (the frontal stage), precipitation was concentrated in the northeastern part due to warm frontogenesis and a quasi-geostrophic ascent. Whereas these dynamics were similar to those of ordinary extratropical cyclones, a warm frontogenesis was dominant over a cold frontogenesis in Hagibis, which was consistent with previous studies of ET. In contrast to an ET case with a frontogenesis due to a juxtaposition of a warm-core TC and a cold-core upper-tropospheric trough (Atallah et al. 2007; Galarneau et al. 2013), a warm frontogenesis in Hagibis appeared to result from the deformation effect due to an interaction between a TC and a relatively uniform baroclinic zone to the north (Keyser et al. 1988).

When Hagibis was moderately distant from the baroclinic zone around 11 October (the prefrontal stage), on the other hand, precipitation was concentrated in the northern part, which was not explained by warm frontogenesis or a quasi-geostrophic ascent. In the outer region, the precipitation was associated with the slantwise vertical motion, consisting of northward (outward) ascending motion with condensational heating and southward (inward) descending motion beneath it with evaporative cooling. This slantwise motion developed within the strong westerly vertical shear that was enhanced between Hagibis and the westerly jet stream. Our analyses of the PV and absolute angular momentum indicated that the slantwise motion in the lower and middle troposphere occurred in an environment with reduced moist symmetric stability accompanied by inertial instability in the upper troposphere and conditional instability in the lower troposphere. As only a few studies have analyzed the symmetric stability in TCs during ET (Colle 2003; Kitabatake 2008; Powell and Bell 2019), our study provides additional insights particularly in the context of the influence of the westerly jet stream.

We have demonstrated that several mechanisms can work during ET. Individual mechanisms should be carefully examined based on their scales, structures, and dynamics, because different mechanisms may result in partially similar characteristics such as the slantwise motion on the tilted isentropic surface, downshear-left precipitation, and left-of-track precipitation. Also note that there was no distinct boundary between the prefrontal and frontal stages (Figs. 5, 6, 7); it appears that multiple processes affected the asymmetric structures of Hagibis simultaneously, changing their contributions gradually. Because ET events in the real atmosphere including Hagibis are more or less affected by tempo-spatially varying environments and various processes, the proposed dynamics should be assessed more precisely based on idealized experiments.

Data Availability Statement

The JMA best track product is available at https://www.jma.go.jp/jma/jma-eng/jma-center/rsmc-hp-pub-eg/besttrack.html. The JRA-55 reanalysis is available at https://jra.kishou.go.jp/JRA-55/index_en.html. The observations, analysis, and a numerical model of JMA are made available under a contact with JMA, because these are basically collected and developed for the operational purpose. The 10-km-grid dataset for the CTL experiment is available in J-STAGE Data. https://doi.org/10.34474/data.jmsj.xxxxxxx. The other output data from the numerical simulations have been archived and are available upon request to the corresponding author.

Supplements

Supplement 1 presents the Q vector analysis using the JRA-55 reanalysis. Supplement 2 presents additional analyses for the CTL experiment. Supplement 3 presents additional analyses for the NIS experiment. Supplement 4 presents the results of additional sensitivity experiment, NEV, in which evaporation of precipitating water was suppressed.

Acknowledgements

We acknowledge helpful comments by Drs. Naoko Kitabatake, Tetsuya Takemi, Julian F. Quinting, Hiroshi Niino, Ryuichi Kawamura, Akira Kuwano-Yoshida, Hironori Fudeyasu, Kosuke Ito, Eigo Tochimoto, Shun-Ichi Watanabe, Hidetaka Hirata, Nao Takamura, Takeshi Enomoto, and anonymous reviewers. The experiments were conducted using Fujitsu Server PRIMERGY CX2550 in the Meteorological Research Institute. This research was partly supported by JSPS KAKENHI Grants 19H05696, 19H00705, 19K24678, 21H01164 and by the Cooperative Program (No. 143, 2020) of Atmosphere and Ocean Research Institute, The University of Tokyo.

Appendix

A. Absolute angular momentum analysis

Absolute angular momentum (AAM) diagnoses symmetric instability. The AAM about the cyclone center (M_c) is defined as

$$M_c = r_c v_c + \frac{1}{2} f_c r_c^2, \tag{A.1}$$

where r_c is the radius from the cyclone center, v_c is the azimuthal wind, and f_c is the Coriolis parameter at the cyclone center. In addition, the AAM about the axis of Earth's rotation (M_e) is defined as

$$M_e = a\cos\phi(a\omega_e\cos\phi + u), \tag{A.2}$$

where a is Earth's radius, ϕ is latitude, ω_e is the angular speed of Earth's rotation, and u is the zonal wind. Although balanced winds are preferable for analyzing AAM, a geostrophic wind does not provide a good approximation around a TC, and a gradient wind is indeterminate for a strong anticyclonic flow as shown in Fig. 13e. As an alternative, we utilized the non-divergent wind, because the balanced winds at least exclude the divergent component.

The surface of AAM is compared with the surface of SEPT and potential temperature to diagnose moist and dry symmetric instability, respectively, (Schultz and Schumacher 1999). If the AAM surface becomes more (less) horizontal owing to strong (weak) vertical shear, symmetric stability decreases (increases). In particular, an AAM surface that is parallel to the SEPT surface denotes moist symmetric neutrality, which is assumed in the axisymmetric dynamics of a TC in Emanuel (1986). Furthermore, an AAM surface that is more horizontal than the SEPT surface denotes moist symmetric instability (Black et al. 1994; Schultz and Schumacher 1999).

If we consider the cylindrical coordinates around the cyclone center, Fig. 14a can be regarded as the radial-vertical distribution of the azimuthal wind, where M_c in Eq. (A.1) is conserved. Figure 16a shows the meridional-vertical distribution of M_c and SEPT; unsaturated areas are masked because moist symmetric stability is only applicable to saturated conditions. The isolines of M_c on the north side of Hagibis were more horizontal than those on the south side because of the strong vertical shear. In particular, around 2°–4° north of the cyclone center in the lower and middle troposphere, the isolines of M_c were nearly parallel to or more horizontal than those of SEPT, implying moist symmetric neutrality or instability. These results indicate that the north side of Hagibis was more favorable for slantwise ascending motion than the south side. Fig. 16

Because the assumption that the flow perpendicular to the meridional-vertical plane in Fig. 14a was axisymmetric about the cyclone center may not provide a good approximation of the horizontal flow distant from Hagibis, we also examined the moist symmetric stability based on the assumption that the flow was uniform in the zonal direction, where M_e in Eq. (A.2) is conserved. The meridional-vertical distribution of M_e and SEPT (Fig. 16b) shows that on the north side of Hagibis, the isolines of M_e again were nearly parallel to or more horizontal than those of SEPT. Thus, under both assumptions, axisymmetry about the cyclone center and axisymmetry about Earth's axis (zonal symmetry), the north side of Hagibis was accompanied by reduced moist symmetric stability compared to the south side.

We discuss what atmospheric variables determine the slopes of M_c and

M_e. Because the AAM (M) surface satisfies

$$\delta M = \frac{\partial M}{\partial y}\delta y + \frac{\partial M}{\partial z}\delta z = 0, \tag{A.3}$$

the slope of the AAM surface is given by

$$\left(\frac{\delta z}{\delta y}\right)_M = -\left(\frac{\partial M}{\partial y}\right) \Big/ \left(\frac{\partial M}{\partial z}\right) \tag{A.4}$$

(e.g. Holton 2004). For M_c to the north of the cyclone on the meridional plane, y corresponds to the radius r_c from the cyclone center. Thus, the partial derivatives of Eq. (A.1) with respect to r_c and z determine the slope of M_c,

$$\left(\frac{\delta z}{\delta y}\right)_{M_c} = -\left(\frac{\partial v_c}{\partial z}\right)^{-1} \left(f_c + \frac{\partial v_c}{\partial r_c} + \frac{v_c}{r_c}\right). \tag{A.5}$$

For M_e on the meridional plane, y corresponds to $a\phi$, and u corresponds to $-v_c$ along the half line running northward from the cyclone center. Thus, the partial derivatives of Eq. (A.2) with respect to $a\phi$ and z determine the slope of M_e,

$$\left(\frac{\delta z}{\delta y}\right)_{M_e} = -\left(\frac{\partial v_c}{\partial z}\right)^{-1} \left(f_c + \frac{\partial v_c}{\partial r_c} - \frac{v_c}{a}\tan\phi\right), \tag{A.6}$$

where f_c approximates the Coriolis parameter ($2\omega_e \sin\phi$). Note that the second parenthetical terms on the right-hand sides of Eqs. (A.5) and (A.6) are identical to absolute vorticity, which is positive in the Northern Hemisphere except in regions of inertial instability. Given $\frac{\partial v_c}{\partial z}$ is negative on the north side of the cyclone owing to westerly vertical shear, the isolines slope northward with height (Fig. 16a, b).

Subtracting Eq. (A.6) from Eq. (A.5), the difference in slope between M_c and M_e is

$$\left(\frac{\delta z}{\delta y}\right)_{M_c} - \left(\frac{\delta z}{\delta y}\right)_{M_e} = -\left(\frac{\partial v_c}{\partial z}\right)^{-1}\left(\frac{1}{r_c} + \frac{\tan\phi}{a}\right)v_c. \tag{A.7}$$

The first parenthetical term on the right-hand side is negative given the westerly vertical shear between Hagibis and the westerly jet stream (Fig. 14a), and the second term is positive in the Northern Hemisphere. Thus, this equation indicates that the direction of azimuthal flow determines which AAM surface is more horizontal between M_c and M_e. Near the cyclone center, positive v_c resulted in $\left(\frac{\delta z}{\delta y}\right)_{M_c}$ being larger than $\left(\frac{\delta z}{\delta y}\right)_{M_e}$; i.e., the isolines of M_e were more horizontal than those of M_c, which was consistent with the distribution of AAM in Fig. 16a, b. In other words, symmetric stability is greater with M_c, so it is more conservative to evaluate instability with M_c. Near the westerly jet stream, on the other hand, negative v_c indicates that the isolines of M_c were more horizontal than those of M_e.

Although this analysis is only applicable to the meridional-vertical plane through the cyclone center, it is useful for understanding the difference in the assumptions behind the use of symmetric stability.

B. Warm frontogenesis in a simplified ET situation

The frontogenesis analysis in section 4.2 indicated that the deformation effect was important for the enhancement of a warm front in Hagibis. This enhancement can occur even in a simplified ET situation. Figure 17 illustrates the deformation effect owing to an axisymmetric vortex as presented by Keyser et al. (1988; their Figs. 8–9) except that the vortex is located on the south side of a zonally uniform baroclinic zone as in usual ET cases. Outside the radius of maximum wind of the Rankine vortex (the black circle), the azimuthal wind decreases in inverse proportion to the radius (black arrows), and the magnitude of the dilatation axes (gray line segments) is large. The dilatation axes make angles of 45° with the radial direction of the vortex. As a result, the angles between the dilatation axes and the isolines of θ are less than 45° in the northeastern and southwestern quadrants, causing frontogenesis (green shading). In the other quadrants, the angles are greater than 45°, causing frontolysis (purple shading). Because the baroclinic zone is located to the north of the vortex, the deformation process is more intense on the north side of the vortex than on the south side. Thus, the frontogenesis is most intense northeast of the vortex. Fig. 17

References

Atallah, E., L. F. Bosart, and A. R. Aiyyer, 2007: Precipitation distribution associated with landfalling tropical cyclones over the Eastern United States. *Mon. Wea. Rev.*, **135**, 2185–2206.

Beljaars, A., 1995: The parametrization of surface fluxes in large-scale models under free convection. *Quart. J. Roy. Meteor. Soc.*, **121**, 255–270.

Black, R., H. Bluestein, and M. Black, 1994: Unusually strong vertical motions in a Caribbean hurricane. *Mon. Wea. Rev.*, **122**, 2722–2739.

Colle, B. A., 2003: Numerical simulations of the extratropical transition of Floyd (1999): Structural evolution and responsible mechanisms for the heavy rainfall over the northeast United States. *Mon. Wea. Rev.*, **131**, 2905–2926.

Dai, Y., S. J. Majumdar, and D. S. Nolan, 2019: The outflow–rainband relationship induced by environmental flow around tropical cyclones. *J. Atmos. Sci.*, **76**, 1845–1863.

Deng, D., and E. A. Ritchie, 2018: Rainfall characteristics of recurving tropical cyclones over the western North Pacific. *J. Climate*, **31**, 575–592.

Emanuel, K. A., 1986: An air-sea interaction theory for tropical cyclones. Part I: steady-state maintenance. *J. Atmos. Sci.*, **43**, 585–604.

Endlich, R. M., 1961: Computation and uses of gradient winds. *Mon. Wea. Rev.*, **89**, 187–191.

Evans, C., K. M. Wood, S. D. Aberson, H. M. Archambault, S. M. Milrad, L. F. Bosart, K. L. Corbosiero, C. A. Davis, J. R. D. Pinto, J. Doyle, C. Fogarty, T. G. Galarneau Jr., C. M. Grams, K. S. Griffin, J. Gyakum, R. E. Hart, K. Naoko, H. S. Lentink, R. McTaggart-Cowan, W. Perrie, J. F. D. Quinting, C. A. Reynolds, M. Riemer, E. A. Ritchie, Y. Sun, and F. Zhang, 2017: The extratropical transition of tropical cyclones. Part I: Cyclone evolution and direct impacts. *Mon. Wea. Rev.*, **145**, 4317–4344.

Evans, J. L., and R. E. Hart, 2003: Objective indicators of the life cycle evolution of extratropical transition for Atlantic tropical cyclones. *Mon. Wea. Rev.*, **131**, 909–925.

Foerster, A. M., M. M. Bell, P. A. Harr, and S. C. Jones, 2014: Observations of the eyewall structure of Typhoon Sinlaku (2008) during the transformation stage of extratropical transition. *Mon. Wea. Rev.*, **142**, 3372–3392.

Galarneau, T. J., C. A. Davis, and M. A. Shapiro, 2013: Intensification of hurricane Sandy (2012) through extratropical warm core seclusion. *Mon. Wea. Rev.*, **141**, 4296–4321.

Harr, P. A., and R. L. Elsberry, 2000: Extratropical transition of tropical cyclones over the western North Pacific. Part I: Evolution of structural characteristics during the transition process. *Mon. Wea. Rev.*, **128**, 2613–2633.

Holton, J. R., 2004: *An introduction to dynamic meteorology* (4 Ed.). Academic Press.

Iizuka, S., R. Kawamura, H. Nakamura, and T. Miyama, 2021: Influence of warm SST in the Oyashio region on rainfall distribution of Typhoon Hagibis (2019). *SOLA*, **17A**, 21–28.

Ishizaki, H., and H. Matsuyama, 2018: Distribution of the annual precipitation ratio of radar/raingauge-analyzed precipitation to AMeDAS across Japan. *SOLA*, **14**, 192–196.

Ito, K., and H. Ichikawa, 2021: Warm ocean accelerating tropical cyclone Hagibis (2019) through interaction with a mid-latitude westerly jet. *SOLA*, **17A**, 1–6.

Japan Aerospace Exploration Agency, 2020: JAXA/EORC tropical cyclone database. `https://sharaku.eorc.jaxa.jp/TYP_DB/data/TYP_DB_GPM/201910/20W/3DDPR.20191011.031918.06A.20W.HAGIBIS.mp4` (Accessed on 22 December 2020).

Japan Meteorological Agency, 2013: Outline of the operational numerical weather prediction at the Japan Meteorological Agency. http://www.jma.go.jp/jma/jma-eng/jma-center/nwp/outline2013-nwp/index.htm (Accessed on 19 January 2021).

Japan Meteorological Agency, 2019: Outline of the operational numerical weather prediction at the Japan Meteorological Agency. http://www.jma.go.jp/jma/jma-eng/jma-center/nwp/outline2019-nwp/index.htm (Accessed on 19 January 2021).

Japan Meteorological Agency, 2020: RSMC best track data. https://www.jma.go.jp/jma/jma-eng/jma-center/rsmc-hp-pub-eg/besttrack.html (Accessed on 4 February 2020).

Jones, S. C., 1995: The evolution of vortices in vertical shear. 1. initially barotropic vortices. *Quart. J. Roy. Meteor. Soc.*, **121**, 821–851.

Jones, S. C., P. A. Harr, J. Abraham, L. F. Bosart, B. J. Bowyer, J. L. Evans, D. E. Hanley, B. N. Hanstrum, R. E. Hart, F. Lalaurette, M. R. Sinclair, R. K. Smith, and C. Thorncroft, 2003: The extratropical transition of tropical cyclones: Forecast challenges, current understanding, and future directions. *Wea. Forecasting*, **18**, 1052–1092.

Katsumata, M., S. Mori, B. Geng, and J. Inoue, 2016: Internal structure of ex-Typhoon Phanfone (2014) under an extratropical transition as observed by the research vessel Mirai. *Geophys. Res. Lett.*, **43**, 9333–9341.

Kawase, H., M. Yamaguchi, Y. Imada, S. Hayashi, A. Murata, T. Nakaegawa, T. Miyasaka, and I. Takayabu, 2021: Enhancement of extremely heavy precipitation induced by Typhoon Hagibis (2019) due to historical warming. *SOLA*, **17A**, 7–13.

Keller, J. H., C. M. Grams, M. Riemer, H. M. Archambault, L. Bosart, J. D. Doyle, J. L. Evans, T. J. Galarneau, K. Griffin, P. A. Harr, N. Kitabatake, R. McTaggart-Cowan, F. Pantillon, J. F. Quinting, C. A. Reynolds, E. A. Ritchie, R. D. Torn, and F. Zhang, 2019: The extratropical transition of tropical cyclones. Part II: Interaction with the midlatitude flow, downstream impacts, and implications for predictability. *Mon. Wea. Rev.*, **147**, 1077–1106.

Keyser, D., M. J. Reeder, and R. J. Reed, 1988: A generalization of Petterssen's frontogenesis function and its relation to the forcing of vertical motion. *Mon. Wea. Rev.*, **116**, 762–781.

Kitabatake, N., 2002: Extratropical transformation of Typhoon Vicki

(9807): Structural change and the role of upper-tropospheric disturbances. *J. Meteor. Soc. Japan*, **80**, 229–247.

Kitabatake, N., 2008: Extratropical transition of Typhoon Tokage (0423) and associated heavy rainfall on the left side of its track over western Japan. *Pap. Meteor. Geophys*, **59**, 97–114.

Kitabatake, N., 2011: Climatology of extratropical transition of tropical cyclones in the western North Pacific defined by using cyclone phase space. *J. Meteor. Soc. Japan*, **89**, 309–325.

Kitabatake, N., S. Hoshino, K. Bessho, and F. Fujibe, 2007: Structure and intensity change of Typhoon Songda (0418) undergoing extratropical transition. *Pap. Meteor. Geophys.*, **58**, 135–153.

Klein, P. M., P. A. Harr, and R. L. Elsberry, 2000: Extratropical transition of western North Pacific tropical cyclones: An overview and conceptual model of the transformation stage. *Wea. Forecasting*, **15**, 373–395.

Knox, J. A., and P. R. Ohmann, 2006: Iterative solutions of the gradient wind equation. *Comput. Geosci.*, **32**, 656–662.

Kobayashi, S., Y. Ota, Y. Harada, A. Ebita, M. Moriya, H. Onoda, K. Onogi, H. Kamahori, C. Kobayashi, H. Endo, K. Miyaoka, and

K. Takahashi, 2015: The JRA-55 Reanalysis: general specifications and basic characteristics. *J. Meteor. Soc. Japan*, **93**, 5–48.

Komaromi, W. A., and J. D. Doyle, 2018: On the dynamics of tropical cyclone and trough interactions. *J. Atmos. Sci.*, **75**, 2687–2709.

Kunii, M., K. Ito, and A. Wada, 2017: Preliminary test of a data assimilation system with a regional high-resolution atmosphere-ocean coupled model based on an ensemble Kalman filter. *Mon. Wea. Rev.*, **145**, 565–581.

Kurihara, Y., T. Sakurai, and K. T., 2006: Global daily sea surface temperature analysis using data from satellite microwave radiometer, satellite infrared radiometer, and in-situ observations (in Japanese). *Wea. Service. Bull.*, **73**, 1–18.

Kwon, Y., and W. Frank, 2008: Dynamic instabilities of simulated hurricane-like vortices and their impacts on the core structure of hurricanes. Part II: Moist experiments. *J. Atmos. Sci.*, **65**, 106–122.

Lentink, H. S., C. M. Grams, M. Riemer, and S. C. Jones, 2018: The effects of orography on the extratropical transition of tropical cyclones: A case study of Typhoon Sinlaku (2008). *Mon. Wea. Rev.*, **146**, 4231–4246.

Lin, Y., R. Farley, and H. Orville, 1983: Bulk parameterization of the snow field in a cloud model. *J. Appl. Meteor.*, **22**, 1065–1092.

Murakami, M., 1990: Numerical modeling of dynamical and microphysical evolution of an isolated convective cloud - The 19 July 1981 CCOPE cloud. *J. Meteor. Soc. Japan*, **68**, 107–128.

Murata, A., 2009: A mechanism for heavy precipitation over the Kii Peninsula accompanying Typhoon Meari (2004). *J. Meteor. Soc. Japan*, **87**, 101–117.

Nakanishi, M., and H. Niino, 2004: An improved Mellor–Yamada level-3 model with condensation physics: Its design and verification. *Boundary Layer Meteorol.*, **112**, 1–31.

Naval Research Laboratory, 2019: NRL tropical cyclone page. `https://www.nrlmry.navy.mil/TC.html` (Accessed on 30 November 2019).

Powell, S. W., and M. M. Bell, 2019: Near-surface frontogenesis and atmospheric instability along the U.S. East Coast during the extratropical transition of Hurricane Matthew (2016). *Mon. Wea. Rev.*, **147**, 719–732.

Quinting, J. F., M. M. Bell, P. A. Harr, and S. C. Jones, 2014: Structural characteristics of T-PARC Typhoon Sinlaku during its extratropical transition. *Mon. Wea. Rev.*, **142**, 1945–1961.

Rappin, E. D., M. C. Morgan, and G. J. Tripoli, 2011: The impact of outflow environment on tropical cyclone intensification and structure. *J. Atmos. Sci.*, **68**, 177–194.

Riemer, M., M. T. Montgomery, and M. E. Nicholls, 2010: A new paradigm for intensity modification of tropical cyclones: thermodynamic impact of vertical wind shear on the inflow layer. *Atmos. Chem. Phys.*, **10**, 3163–3188.

Saito, K., 2019: On the northward ageostrophic winds associated with a tropical cyclone. *SOLA*, **15**, 222–227.

Saito, K., T. Fujita, Y. Yamada, J.-I. Ishida, Y. Kumagai, K. Aranami, S. Ohmori, R. Nagasawa, S. Kumagai, C. Muroi, T. Kato, H. Eito, and Y. Yamazaki, 2006: The operational JMA nonhydrostatic mesoscale model. *Mon. Wea. Rev.*, **134**, 1266–1298.

Schultz, D. M., and C. A. Doswell, III, 1999: Conceptual models of upper-level frontogenesis in south-westerly and north-westerly flow. *Quart. J. Roy. Meteor. Soc.*, **125**, 2535–2562.

Schultz, D. M., and P. N. Schumacher, 1999: The use and misuse of conditional symmetric instability. *Mon. Wea. Rev.*, **127**, 2709–2732.

Shimazu, Y., 1998: Classification of precipitation systems in mature and early weakening stages of typhoons around Japan. *J. Meteor. Soc. Japan*, **76**, 437–445.

Shimoji, K., 2017: Introduction to the Himawari-8 Atmospheric Motion Vector algorithm. *Meteorological Satellite Center Technical Note*, **62**, 73–77.

Takemi, T., and T. Unuma, 2020: Environmental factors for the development of heavy rainfall in the eastern part of Japan during Typhoon Hagibis (2019). *SOLA*, **16**, 30–36.

Ueno, M., 2007: Observational analysis and numerical evaluation of the effects of vertical wind shear on the rainfall asymmetry in the typhoon inner-core region. *J. Meteor. Soc. Japan*, **85**, 115–136.

Ueno, M., 2008: Effects of ambient vertical wind shear on the inner-core asymmetries and vertical tilt of a simulated tropical cyclone. *J. Meteor. Soc. Japan*, **86**, 531–555.

Yanase, W., and H. Niino, 2019: Parameter sweep experiments on a spectrum of cyclones with diabatic and baroclinic processes. *J. Atmos. Sci.*, **76**, 1917–1935.

Yanase, W., U. Shimada, and N. Takamura, 2020: Large-scale conditions for reintensification after the extratropical transition of tropical cyclones in the western North Pacific Ocean. *J. Climate*, **33**, 10039–10053.

List of Figures

(a) 0409 UTC 09 Oct (b) 0804 UTC 11 Oct (c) 1645 UTC 12 Oct

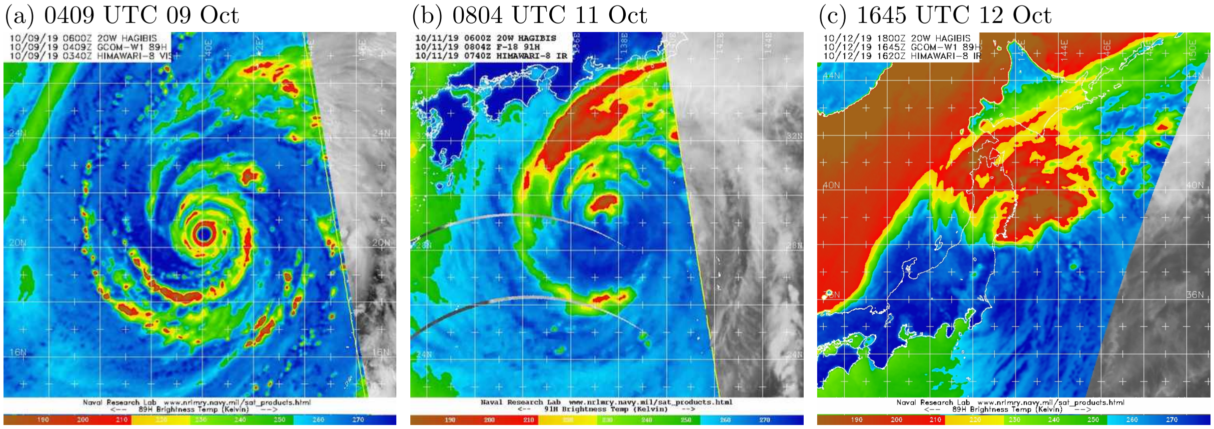

Fig. 1. High-frequency microwave (89–91 GHz) satellite imagery (color shading) for Typhoon Hagibis in 2019. (a) 0409 UTC 09 October, (b) 0804 UTC 11 October, and (c) 1645 UTC 12 October. The gray shadings are visible or infrared satellite imagery at the time close to the microwave imagery. Satellite imagery courtesy of the Naval Research Laboratory (2019).

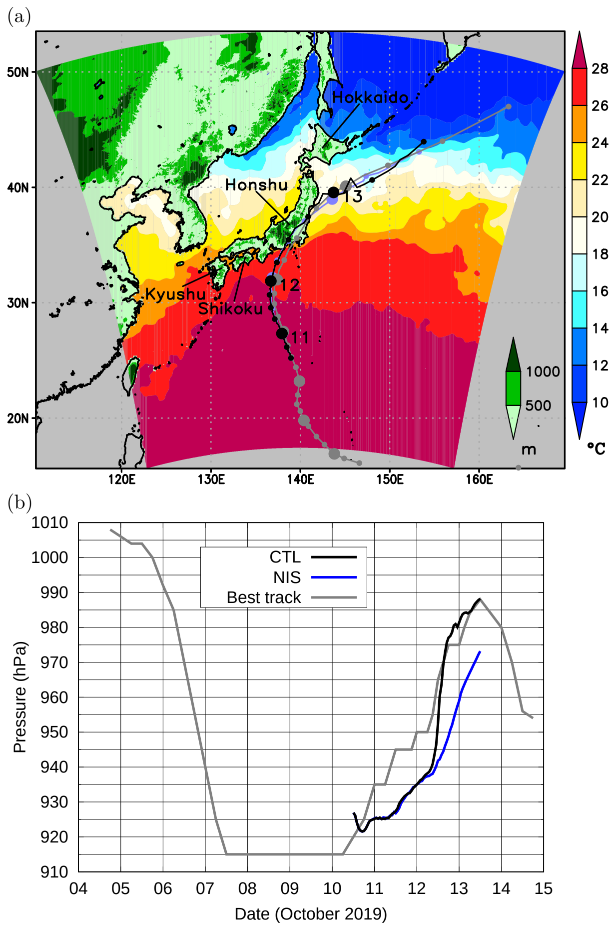

Fig. 2. Life cycles of Hagibis in the CTL (black) and NIS (blue) experiments along with the best track analysis (gray). (a) Tracks with 6-hourly locations (circles; large circles for 0000 UTC) where the digits denote 11, 12, and 13 October 2019. The track for NIS is underneath that for CTL, because the two tracks are similar to each other. Colors represent SST (°C) in ocean areas and ground elevation (m) in land areas in the CTL experiment. (b) Time evolution of minimum sea level pressure of Hagibis

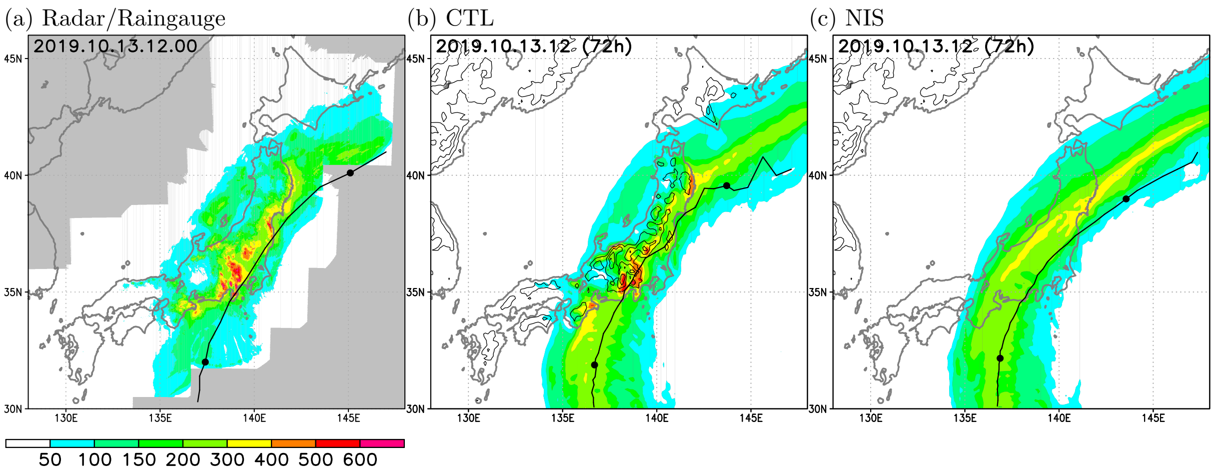

Fig. 3. Total precipitation (mm) accumulated from 1200 UTC 10 October to 1200 UTC 13 October 2019 and tracks of Hagibis: (a) radar/rain gauge-analyzed precipitation (with best track analysis), (b) CTL, and (c) NIS. The black circles indicate the location of Hagibis at 0000 UTC 11 October and 12 October. Contours in (b) and (c) indicate the ground elevation in the respective experiments; contour interval 500 m.

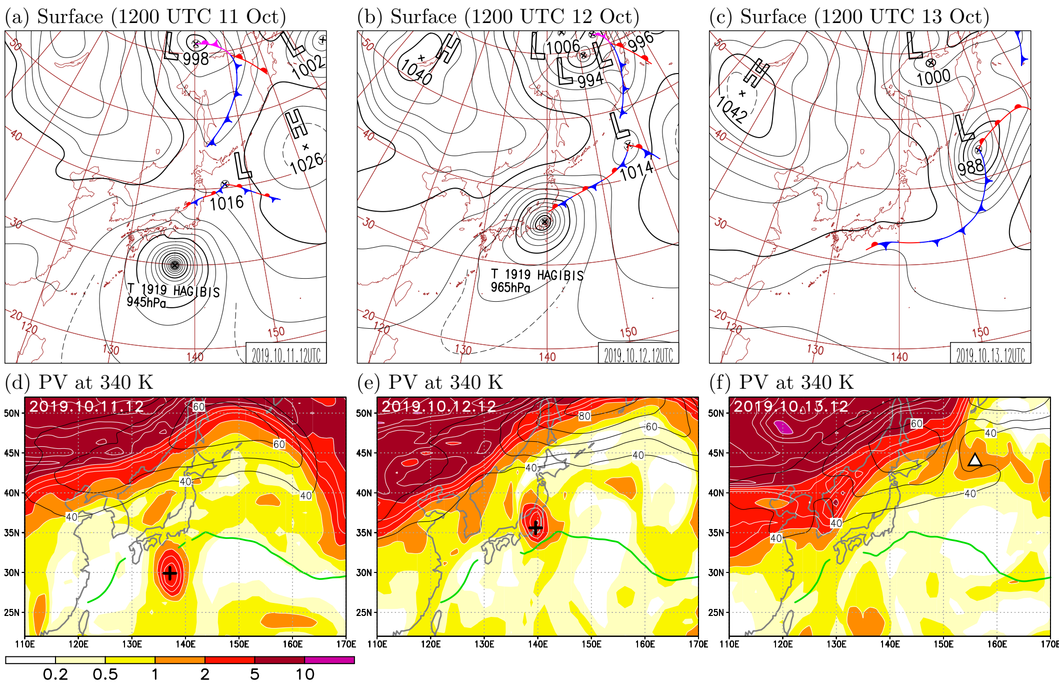

Fig. 4. Synoptic conditions around Hagibis at (a)(d) 1200 UTC 11 October, (b)(e) 1200 UTC 12 October, and (c)(f) 1200 UTC 13 October. (a)–(c) JMA surface weather charts. (d)–(f) Potential vorticity (PVU; colors) and horizontal wind speed exceeding 40 m s^{-1} (contour interval 5 m s^{-1}) at 340 K isentropic surface along with 26.5°C SST (green curves) based on the JRA-55 reanalysis; the symbols indicate the location of Hagibis on 11 and 12 October (crosses) and ex-Hagibis on 13 October (triangle) in the best track analysis.

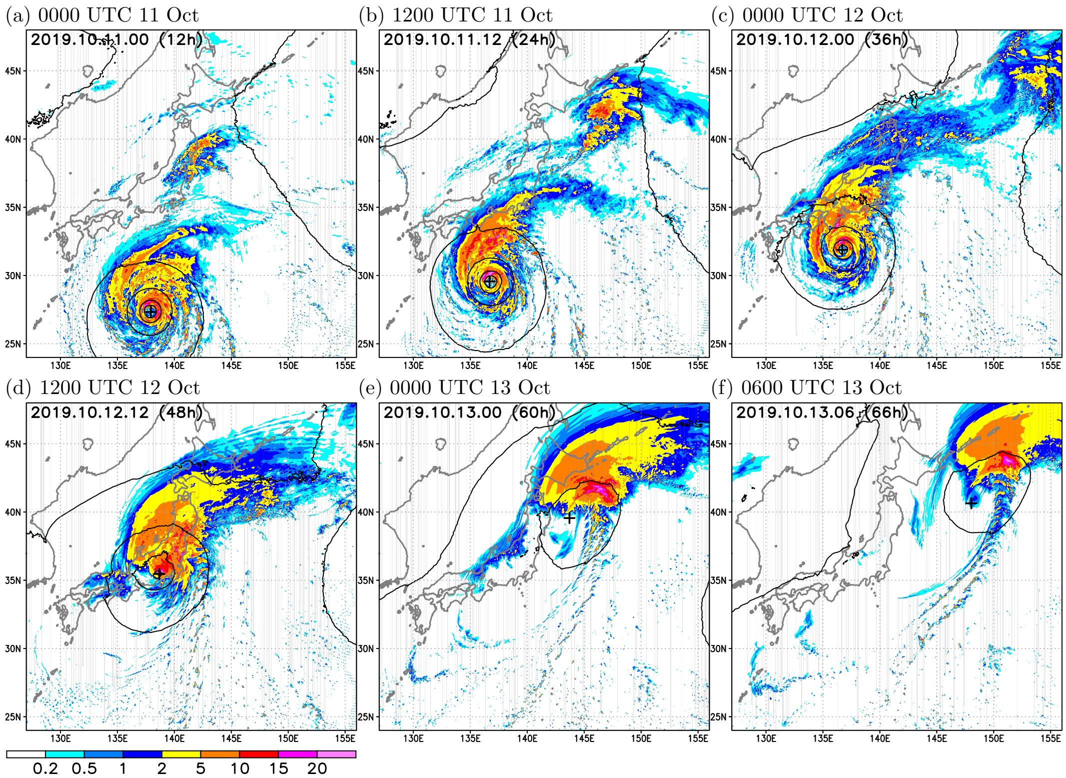

Fig. 5. Total condensed water path (kg m^{-2}; colors) represented in the 2-km-grid dataset in the CTL experiment for (a) 0000 UTC 11 October, (b) 1200 UTC 11 October, (c) 0000 UTC 12 October, (d) 1200 UTC 12 October, (e) 0000 UTC 13 October, and (f) 0600 UTC 13 October. The contours represent sea level pressure at intervals of 20 hPa. The crosses denote the cyclone centers.

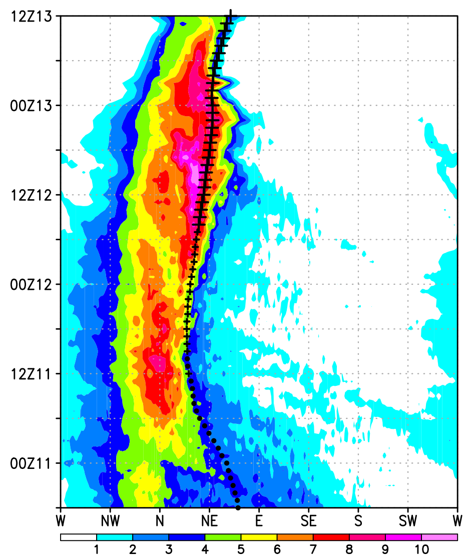

Fig. 6. Azimuth-time Hovmöller diagram of TCWP (kg m^{-2}; colors) averaged over 500 km radius from the cyclone center for the CTL experiment. The symbols denote the direction and magnitude of environmental vertical shear (circles, 0–10 m s^{-1}; small crosses, 10–20 m s^{-1}; large crosses, $>$ 20 m s^{-1}).

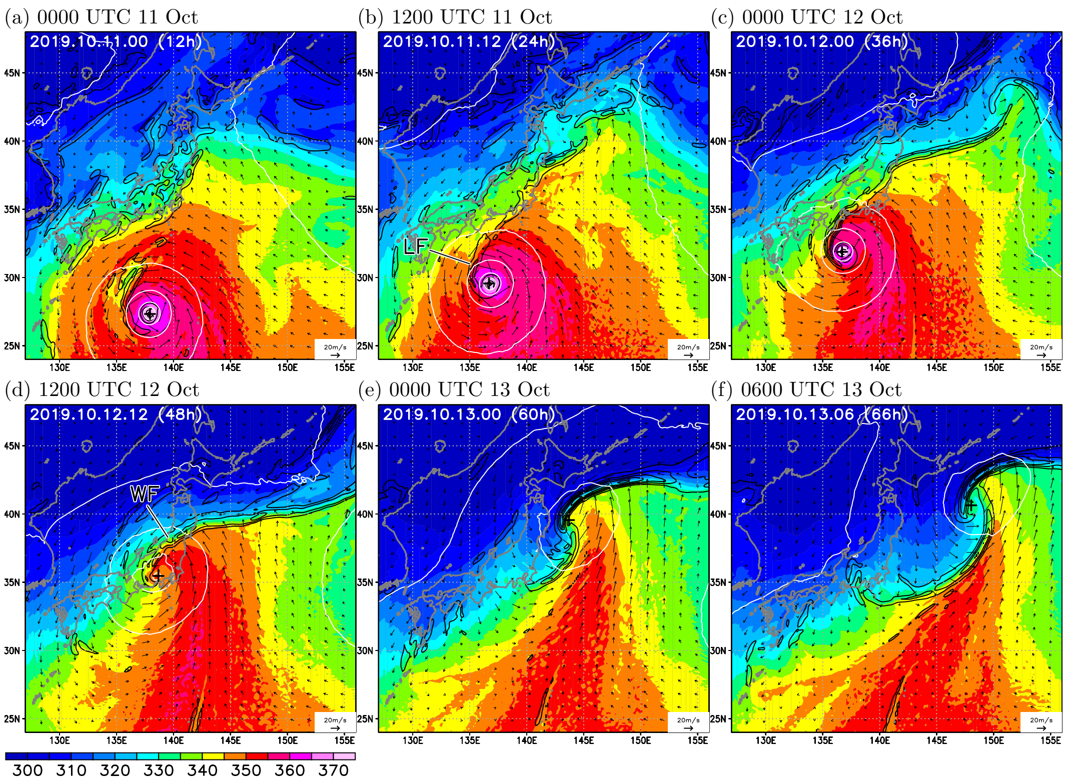

Fig. 7. Equivalent potential temperature (K; colors) at 530 m ASL and the magnitude of its horizontal gradient of EPT (contour interval 1 K (10 km)$^{-1}$) in the CTL experiment for (a) 0000 UTC 11 October, (b) 1200 UTC 11 October, (c) 0000 UTC 12 October, (d) 1200 UTC 12 October, (e) 0000 UTC 13 October, and (f) 0600 UTC 13 October. The white contours represent sea level pressure at intervals of 20 hPa. The labels “LF” in (b) and “WF” in (d) denote the local front and the warm front, respectively. The crosses denote the cyclone centers.

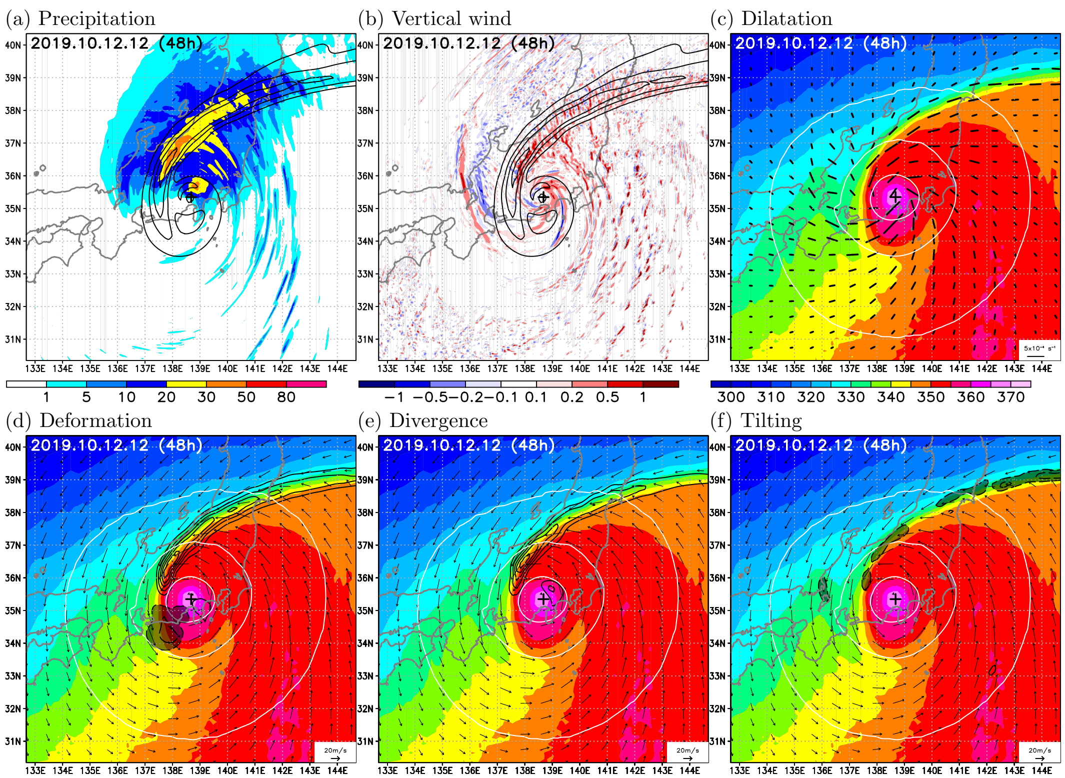

Fig. 8. Frontal dynamics at 1200 UTC 12 October in the NIS experiment. (a) Hourly precipitation (mm); and (b) vertical wind at 530 m ASL (m s^{-1}) in the 2-km-grid dataset; the black contours represent the magnitude of horizontal gradient of EPT at 530 m ASL (contour interval 1 K (10 km)$^{-1}$). (c) Dilatation axes (black line segments) and (d–f) frontogenesis (black contours every 2×10^{-8} K m^{-1} s^{-1}) and frontolysis (dashed contours every -2×10^{-8} K m^{-1} s^{-1} with gray shading) due to (d) deformation, (e) divergence, and (f) tilting effects at 530 m ASL; colors represent EPT (K) and the white contours represent sea level pressure at intervals of 20 hPa. The crosses denote the cyclone centers.

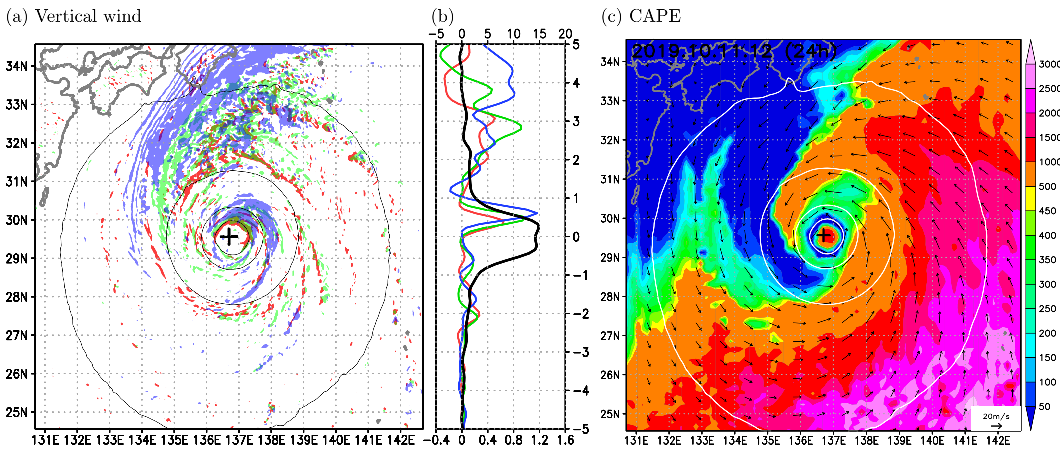

Fig. 9. Horizontal distribution at 1200 UTC 11 October in the CTL experiment. (a) Plan view of vertical wind exceeding 0.5 m s^{-1} in the 2-km-grid dataset at 1944 m (red), 5058 m (transparent green), and 10228 m ASL (transparent blue). (b) Meridional distribution through the cyclone center for the vertical wind (m s^{-1}; labels at the bottom) at 1944 m (red), 5058 m (green), and 10228 m ASL (blue) and density-weighted vertical average of relative vorticity between 1450 and 12130 m ASL (10^{-4} s^{-1}; black; labels at the top) smoothed by a 100-km binomial filter. (c) Plan view of CAPE (m^2 s^{-2}) and horizontal wind vectors at 20 m ASL. The black and white contours in (a) and (c), respectively, represent sea level pressure at intervals of 20 hPa. The center of the cyclone is at the center of the panel; the crosses denote the center in (a) and (c), and the labels on the vertical axis in (b) denotes the latitude relative to the cyclone center.

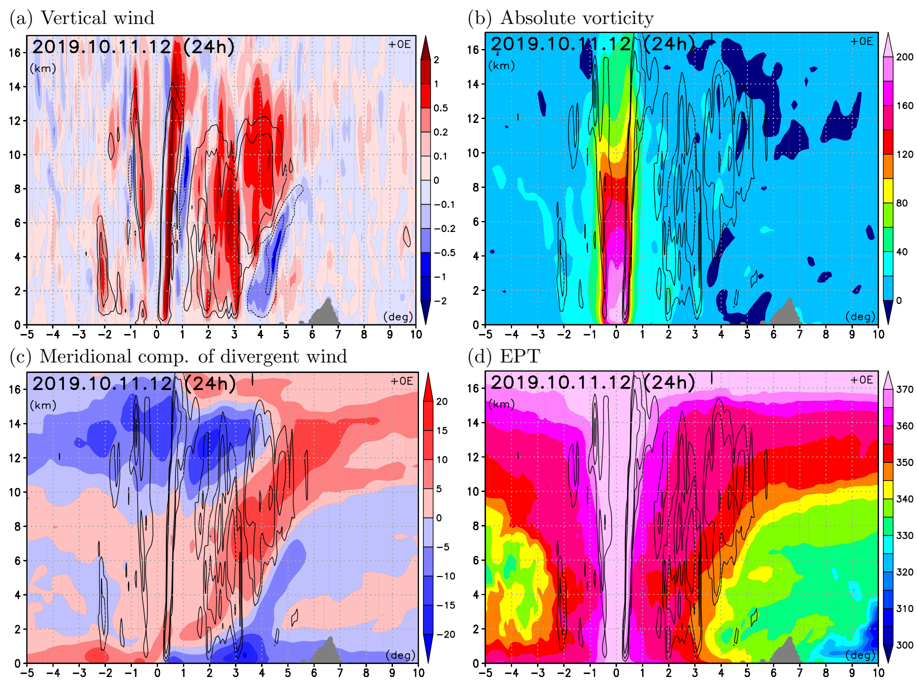

Fig. 10. Meridional-vertical section through the cyclone center at 1200 UTC 11 October in the CTL experiment. (a) Vertical wind (m s^{-1}; colors); the black contours represent diabatic heating of 2 and 5 K h^{-1} (solid contours) and -5 and -2 K h^{-1} (dashed contours). (b) Absolute vorticity (10^{-5} s^{-1}; colors) (c) Meridional component of divergent wind (m s^{-1}; colors). (d) EPT (K; colors). In (b)–(d), the black contours represent updraft of 0.2, 0.5, and 1.0 m s^{-1}. The horizontal axis denotes the latitude relative to the cyclone center.

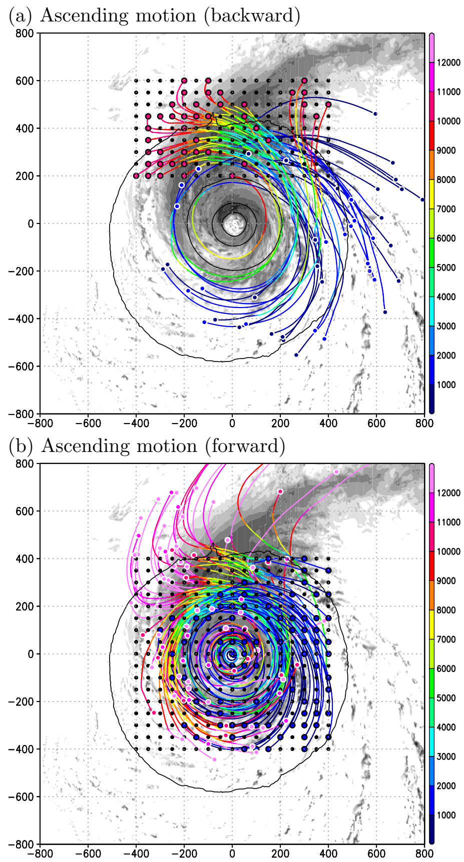

Fig. 11. Trajectories computed for 12 h that started at 1200 UTC 11 October and ended at 0000 UTC 11 October and 0000 UTC 12 October for backward and forward analyses, respectively, in the CTL experiment. (a) Backward trajectories that started at 10 km ASL north of the cyclone center and ended below 2 km ASL. (b) Forward trajectories that started at 1 km ASL around the cyclone center and ended above 10 km ASL. The colors of the trajectories indicate their height (m). The black and white open circles denote the start and end points, respectively; the black dots denote the start points of the trajectories that did not satisfy the criteria for the vertical motion. The horizontal and vertical axes are distances (km) from the cyclone center in the coordinate system relative to the cyclone motion. The gray shading represents TCWP (refer to Fig. 5b) and the contours represent sea level pressure at 1200 UTC 11 October at intervals of 20 hPa.

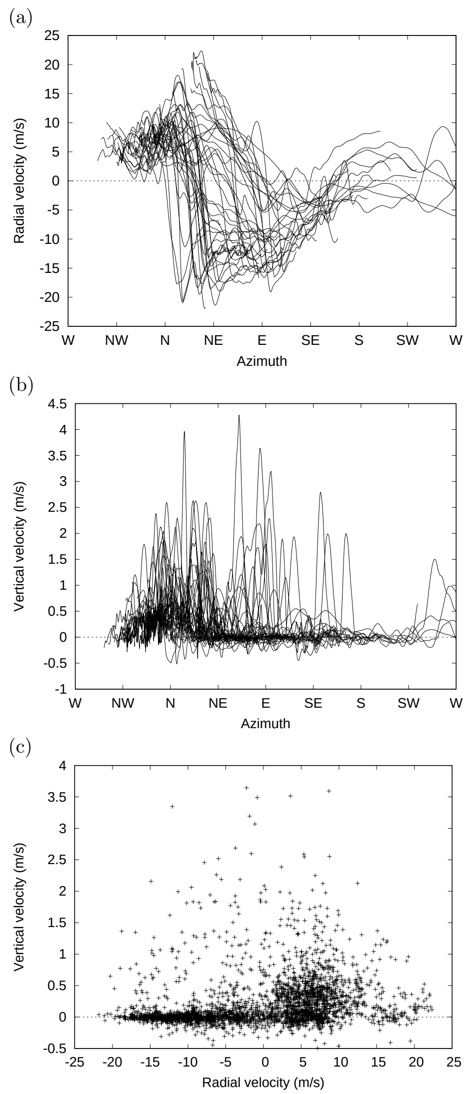

Fig. 12. Locations and velocities relative to the cyclone motion of the backward trajectory parcels in Fig. 11a. (a) Azimuthal locations and radial velocities (m s^{-1}). (b) Azimuthal locations and vertical velocities (m s^{-1}). (c) Radial velocities and vertical velocities sampled every 10 min.

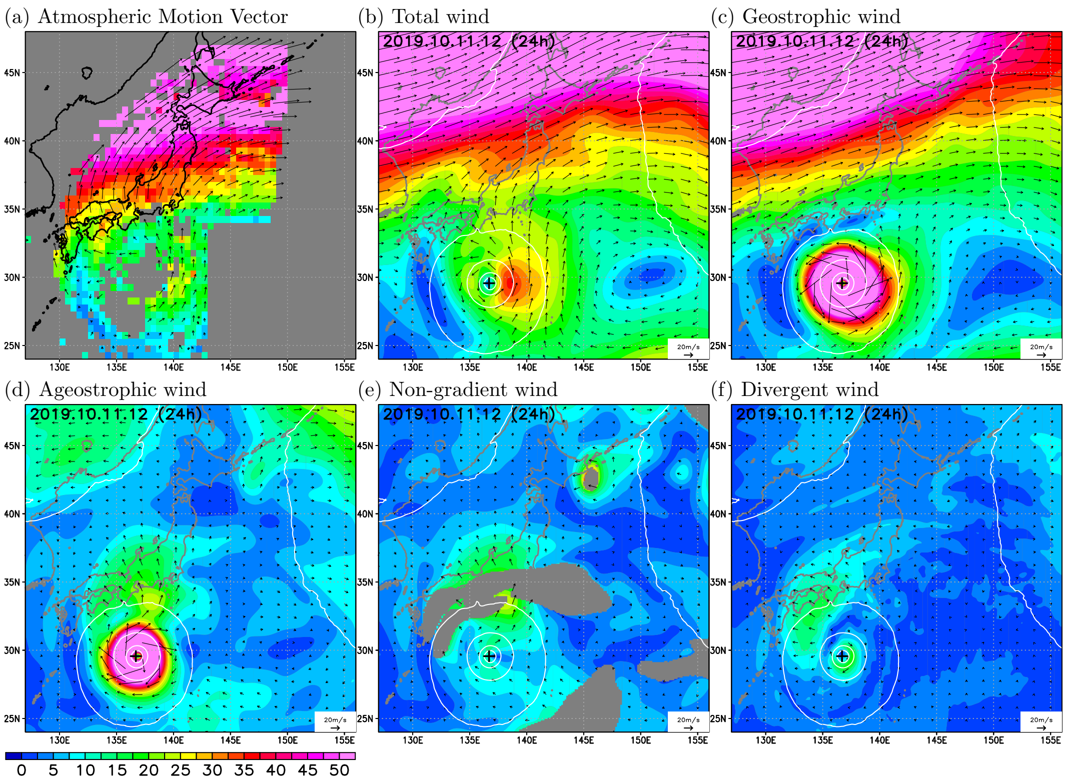

Fig. 13. Horizontal wind vectors and speed (m s^{-1}; colors) in the upper troposphere at 1200 UTC 11 October. (a) Atmospheric motion vector between 200 and 300 hPa derived from Himawari-8 satellite observations. (b) Total wind, (c) geostrophic wind, (d) ageostrophic wind, (e) non-gradient wind (indeterminate where shaded gray), and (f) divergent wind at 10228 m ASL in the CTL experiment. The crosses denote the cyclone centers.

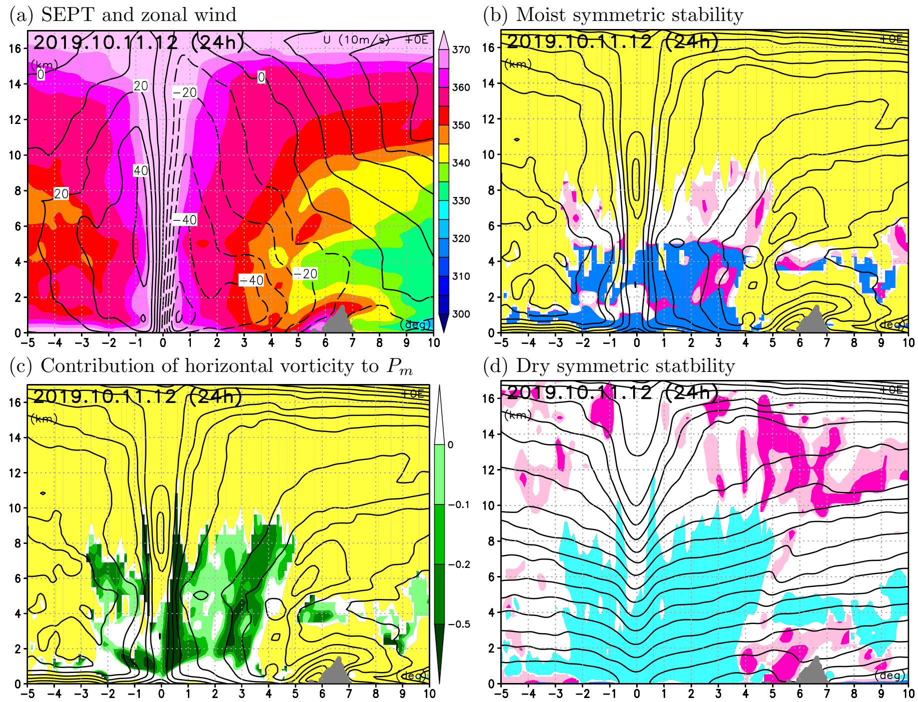

Fig. 14. Meridional-vertical section through the cyclone center in the CTL experiment at 1200 UTC 11 October 2019. (a) SEPT (K; colors) and zonal component of the non-divergent wind (contour interval 10 m s^{-1}); (b) moist symmetric instability ($P_m < 0$ PVU; dark magenta), weak moist symmetric stability ($0 < P_m < 0.2$ PVU; light magenta), conditional instability (blue), and SEPT (contour interval 5 K). (c) Contribution of horizontal vorticity to P_m (PVU; colors), and SEPT (contour interval 5 K). (d) dry symmetric instability ($P_d < 0$ PVU; dark magenta shading), weak dry symmetric stability ($0 < P_d < 0.2$ PVU; light magenta shading), and potential temperature (contours every 5 K). Unsaturated areas (relative humidity < 90 %) are masked in yellow in (b) and (c), and nearly saturated areas (relative humidity > 90 %) are masked in cyan in (d). The horizontal axis denotes the latitude relative to the cyclone center.

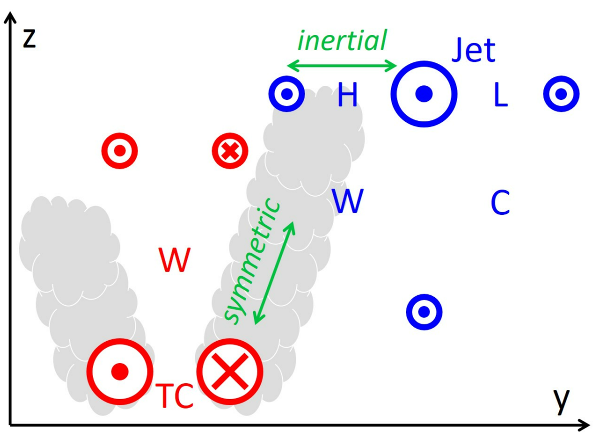

Fig. 15. Schematic profile illustrating the possible atmospheric motions (green arrows) associated with a combination of a TC (red marks) and a westerly jet stream (blue marks) in a meridional-vertical section. The circled dots and circled crosses denote westerly and easterly winds, respectively; larger marks indicate stronger wind. H, anticyclonic horizontal shear; L, cyclonic shear; W, warm anomaly relative to the horizontal mean; C, cold anomaly; "inertial," atmospheric motion enhanced by reduced inertial stability; "symmetric" atmospheric motion enhanced by reduced symmetric stability.

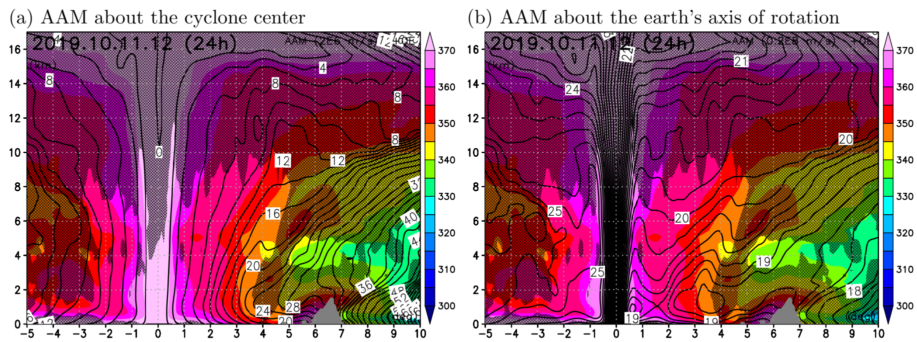

Fig. 16. Meridional-vertical section through the cyclone center in the CTL experiment at 1200 UTC 11 October 2019. (a) AAM about the cyclone center (contour interval 2 $\times$ 10^6 m^2 s^{-1}) and SEPT (K; colors); (b) AAM about Earth's axis of rotation (contour interval 0.2 $\times$ 10^8 m^2 s^{-1}) and SEPT (K; colors); Unsaturated areas (relative humidity < 90 %) are masked in black hatching. The horizontal axis denotes the latitude relative to the cyclone center.

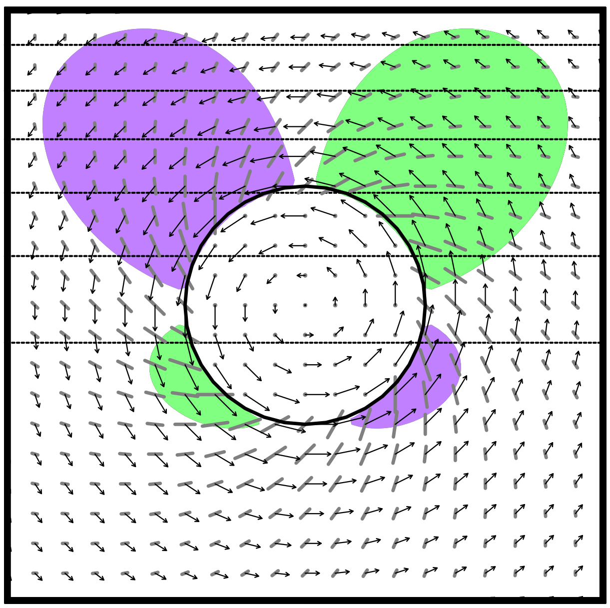

Fig. 17. Schematic illustration showing a plan view of frontogenesis (green) and frontolysis (purple) caused by a Rankine vortex south of a baroclinic zone. The black vectors are horizontal wind associated with the vortex, and the gray line segments are dilatation axes. The black circle denotes the radius of maximum wind of the vortex. The dotted lines are isolines of θ (potential temperature or EPT), indicating that the meridional gradient of θ is steeper north of the vortex.